MSDE

PAPER

View Article Online
View Journal | View Issue

Cite this: *Mol. Syst. Des. Eng.*, 2022, 7, 899

Synthesis of SOT-OH and its application as a building block for the synthesis of new dimeric and trimeric Spiro-OMeTAD materials†

Michele Cariello, ‡[a] Namrata Pant, ‡[a] Alexander H. Harkiss, ‡[a] Frances M. Tracey, [a] Joseph Cameron, [a] Peter J. Skabara, [a] Peter J. Holliman, [b] Pablo Docampo *[a] and Graeme Cooke *[a]

Received 11th March 2022,
Accepted 13th April 2022

DOI: 10.1039/d2me00038e

rsc.li/molecular-engineering

Spiro-OMeTAD has become a ubiquitous hole-transporting material (HTM) in perovskite-based solar cells. However, it has several intrinsic drawbacks including its long-term stability, low conductivity and hole-mobility. Hence, the synthesis of new derivatives with improved charge transporting properties remains an important goal. Here, we have devised a novel synthetic route to prepare unsymmetrically functionalised **Spiro-OMeTAD** derivatives. We report the synthesis of a mono-demethylated **Spiro-OMeTAD** derivative, **SOT-OH**, utilising two different synthetic protocols and show two new derivatives, a dimer (**SOT-D**) and a trimer (**SOT-T**) as exemplars. We fully characterise the developed materials and show significantly higher conductivity values than **Spiro-OMeTAD** when doped with standard ionic salts at the same concentrations. The solar cells fabricated using the mixed composition $Cs_{0.05}(FA_{0.85}MA_{0.15})_{0.95}PbI_3$ perovskite and the novel **SOT-D** show power conversion efficiencies of up to 16.4% under standard AM1.5 illumination compared to 16.1% observed when using the benchmark **Spiro-OMeTAD**.

Design, System, Application

We have designed methodology to reliably and conveniently synthesise a new asymmetric **Spiro-OMeTAD** building block (**SOT-OH**) using both top-down and bottom-up procedures. As exemplars, we have synthesised a dimer (**SOT-D**) and a trimer (**SOT-T**) from **SOT-OH** and have shown that these materials have higher conductivities, and in the case of **SOT-D** a higher power conversion efficiency, than **Spiro-OMeTAD**, which we attribute to the more porous morphology of their films. This work not only provides new methodology for creating unsymmetrically functionalised **Spiro-OMeTAD** derivatives, which will allow exciting new HTMs to be prepared for perovskite and solid-state dye-sensitised solar cells, but also indicates that a more porous HTM film architecture may be advantageous in developing better performing devices.

Introduction

Since its first use as a hole-transporting material (HTM) in solid-state dye-sensitised solar cells (ss-DSSCs)[1] **Spiro-OMeTAD** has become the benchmark HTM for ss-DSSCs. Importantly, this molecule has also become the HTM of choice for perovskite-based solar cells (PSCs)[2,3] which, since 2012, have surpassed the efficiency of any other emerging solar device by achieving a certified record efficiency of 25.7%.[4] Although **Spiro-OMeTAD** has a relatively poor hole-mobility, it can be improved upon doping,[5,6] and has several properties ideal for use as a HTM including energy levels with an appropriate over-potential for typical absorbers (either perovskite or dye), good visible light transparency and electrochemical stability. Furthermore, the high solubility and relatively high glass transition temperature (T_g) contribute to its excellent processability and good morphological properties, which promote pore filling of the mesoporous TiO_2 layer.[7] This blend of properties arises from the combination of the spiro centre, diphenylamine donor groups and methoxy ether substituents. However, the >20 years of research since its first report have shown it difficult to improve on the **Spiro-OMeTAD** core design, suggesting this is close to optimal for this HTM family.

Nevertheless, **Spiro-OMeTAD** is not the perfect HTM owing to the high production costs, inconsistent batch-to-batch purity and low conductivities. Even film morphology, a strength in its as-made devices, limits device durability, as device performance of **Spiro-OMeTAD**-based PSCs has been reported to deteriorate at temperatures above 50 °C.[8–10] This has been ascribed to phenomena such as iodine diffusion from the perovskite layer (in PSCs)[9] and crystallisation,

[a] *School of Chemistry, Joseph Black Building, University of Glasgow, Glasgow, G12 8QQ, UK. E-mail: graeme.cooke@glasgow.ac.uk*
[b] *College of Engineering, Bay Campus, Swansea University, Swansea, SA1 8EN, UK*

† Electronic supplementary information (ESI) available. See DOI: https://doi.org/10.1039/d2me00038e

‡ These authors contributed equally to this manuscript.

especially after annealing.[10,11] Additionally, additives such as *tert*-butylpyridine (*t*BP) which are added to balance the drop in the conduction band edge position of TiO_2 after addition of lithium-based salts in ssDSCs or passivate the perovskite layer in PSCs, have been directly shown to evaporate from the **Spiro-OMeTAD** film causing further device degradation by formation of pinholes.[7,12] These changes hint at the importance of molecular packing within HTM films which arise from the key design feature of the spiro unit at the centre of every **Spiro-OMeTAD** molecule. So, whilst this facilitates ionic movement within films which aids conductivity, dopant loss or indeed rearrangement of **Spiro-OMeTAD** molecules within HTM films is not desirable for device longevity. In this work, we have explored maintaining the **Spiro-OMeTAD** motif but doubling or trebling the molecular weight to hinder intra-film molecular movement.

Since the crystallisation is facilitated by the symmetry of the molecule, Getautis and co-workers demonstrated that making **Spiro-OMeTAD** more unsymmetric improves its mechanical stability without significantly affecting its optoelectronic properties.[11] The introduction of a methyl group to each diphenylamine peripheral unit significantly increased device stability, with 90% of the efficiency retained after 1000 hours of light exposure at 60 °C. This result was followed by more systematic studies of unsymmetric **Spiro-OMeTAD** analogues, changing both the position[13,14] and the type of peripheral heteroatoms.[15] These changes also improved thermal properties and hydrophobicity, with minimal impact on the spectro-electrochemical properties of the HTM.[13,14] More complex modifications involving the central core of **Spiro-OMeTAD** have been investigated by several research groups.[16–19]

Small molecules having completely different properties,[20,21] which sometimes outperform **Spiro-OMeTAD**, have been reported, while significant improvements have been made using polymeric HTMs,[22–25] metal–organic[26–28] or inorganic HTMs.[29,30] Here, we report the synthesis of **SOT-OH**, which serves as a novel building block, due to its reactive hydroxyl group, for the synthesis of new derivatives. Two synthetic approaches using top-down and bottom-up synthetic protocols to furnish **SOT-OH** are described. Furthermore, we report the synthesis of two new **Spiro-OMeTAD** derivatives, **SOT-D** and **SOT-T**, having identical optoelectronic properties to the parent material but different thermal properties and *circa* double or treble the molecular mass, respectively.

Results and discussion

Two different synthetic routes were developed. In our top-down approach (route A, Scheme 1 and ESI†), **SOT-OH** was synthesised from commercially available **Spiro-OMeTAD**. Various demethylation procedures were attempted (Table S1, ESI†), with the most successful conditions being a sodium bis(trimethylsilyl)amide ($NaN(SiMe_3)_2$) mediated demethylation in 1,3-dimethyl-2-imidazolidinone (DMI) at 185 °C.[31] This convenient one-step approach proved

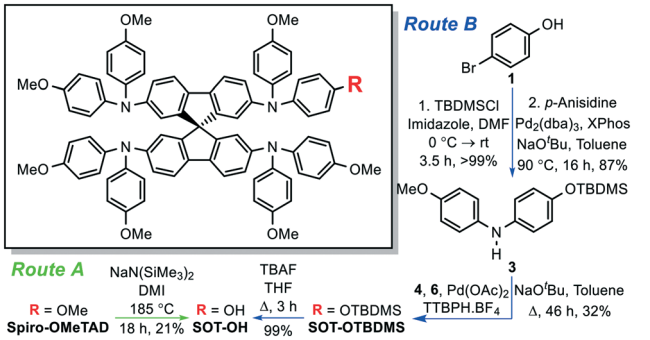

Scheme 1 Synthesis of **SOT-OH** *via* route A (1 step) and route B (4 steps).

effective for the small scale (~50 mg) synthesis of **SOT-OH**, whereas for large scales, our bottom-up protocol (route B, Scheme 1) proved to be very robust. This route commenced with inexpensive 4-bromophenol **1**, which underwent quantitative hydroxy-protection using a *tert*-butyldimethylsilyl (TBDMS) group under standard conditions to produce compound **2**. A Buchwald–Hartwig cross-coupling reaction with *p*-anisidine was then employed to obtain the TBDMS-protected diphenylamine **3**. Next, a one-pot Buchwald–Hartwig cross-coupling between **3**, 4,4′-dimethyoxydiphenylamine **4**, and 2,2′,7,7′-tetrabromo-9,9′-spirobifluorene **6** produced consistent 32% yields of mono-TBDMS-protected **SOT-OTBDMS**. Despite the moderate yield, this process is scalable (>1 g) and highly reproducible. The other major product of this reaction is **Spiro-OMeTAD** which suggests that symmetrical diphenylamine **4** is more active under the reaction conditions in comparison to the TBDMS-protected diphenylamine **3**. The final step to form **SOT-OH** involved the removal of the protecting group *via* tetrabutylammonium fluoride (TBAF). Full experimental details are reported in the ESI.†

Using the desired building block **SOT-OH**, we investigated its reactivity by synthesising exemplar dimer and trimer derivatives, **SOT-D** and **SOT-T**, respectively. Assemblies of this type were selected to both indicate the potential synthetic applications of **SOT-OH** and provide new materials that will retain the advantages of **Spiro-OMeTAD** whilst providing materials with potentially enhanced thermal and morphological properties. Hydroquinone **7** and phloroglucinol **9** were chosen as linker groups due to their commercial availability and structural simplicity (Scheme 2). Both compounds were subjected to standard Williamson ether synthesis conditions using sodium hydride and 1,6-dibromohexane to install the brominated hexyl chain on each derivative. Hexyl chains were selected in this study as it was hypothesised that, if shorter alkyl chains were used, then steric hindrance between the bulky spiro units could lead to poor conversion towards the target materials. The obtained alkyl bromide intermediates **8** and **10** underwent Williamson ether synthesis with **SOT-OH**, to yield the desired dimer **SOT-D** and trimer **SOT-T** materials in 51% and 57% yields, respectively (detailed synthesis provided in the ESI†).

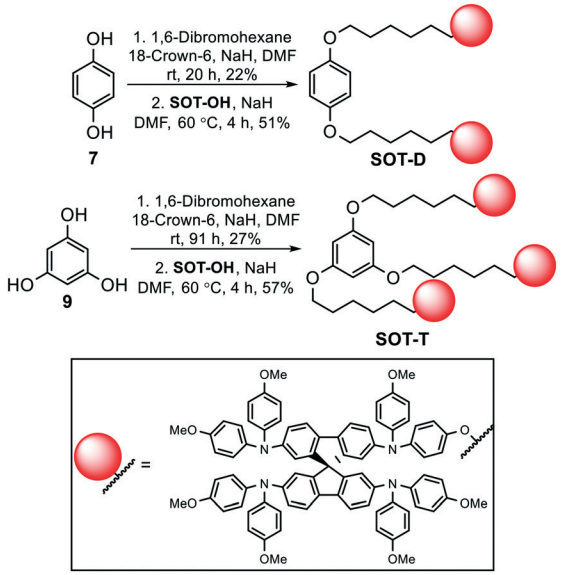

Scheme 2 Synthesis of dimer **SOT-D** and trimer **SOT-T** materials.

To maximise the light harvesting of perovskite/dye absorbers, HTM light absorption between 400–800 nm should be minimised. The absorption and emission spectra for **SOT-D** and **SOT-T** were recorded in dichloromethane and compared with **Spiro-OMeTAD** (Fig. 1). The λ_{max} for **SOT-D** and **SOT-T** are both observed at 386 nm, which is similar to the λ_{max} for **Spiro-OMeTAD** (384 nm) and correspond to their π–π^* electron transitions.[32,33] The extinction coefficients increase on going from **Spiro-OMeTAD** to **SOT-T** due to the increased number of **Spiro-OMeTAD** units per molecule. However, importantly for light harvesting, no red shift into the visible range is observed and all three molecules have an identical cut-off wavelength of 420 nm, corresponding to an optical energy gap ($E_{g,opt}$) of ~2.95 eV. This phenomenon arises from the molecular design of these new HTMs whereby separate **Spiro-OMeTAD** units are connected through non-conjugated linkers, which effectively means each **Spiro-OMeTAD** unit behaves as a separate HTM unit regardless of whether present within the monomeric **Spiro-OMeTAD**, dimeric **SOT-D** or trimeric **SOT-T**. The emission spectra of **Spiro-OMeTAD**, **SOT-D** and **SOT-T** originate from the π^*–π transition. The maximum emission wavelength of the three materials is again very similar at 424, 427 and 427 nm, respectively. Due to the analogous absorption and emission spectra, the Stokes shift values were almost identical (40 nm), for the same reasons described above.

Electrochemical analysis of **SOT-D** and **SOT-T** in dichloromethane was carried out *via* cyclic voltammetry (CV) and square wave voltammetry (SWV) and the results were compared with **Spiro-OMeTAD**,[34] under the same conditions. As the CVs indicate (Fig. 2), **SOT-D** and **SOT-T** both undergo three main oxidations, identical to **Spiro-OMeTAD**,[35] confirming that the alkyl chains that connect the terminal units are long enough to prevent intramolecular charge transfer between spiro units. Although the peak currents increase in line with increasing spiro units on going from **Spiro-OMeTAD**, **SOT-D** to **SOT-T**, the shape of the curves are almost identical suggesting that, similarly to **Spiro-OMeTAD**, the first oxidation events (grey shaded area, Fig. 2) are likely the result of two reversible one-electron oxidations of the diarylamine subunits. Finally, the third more prominent

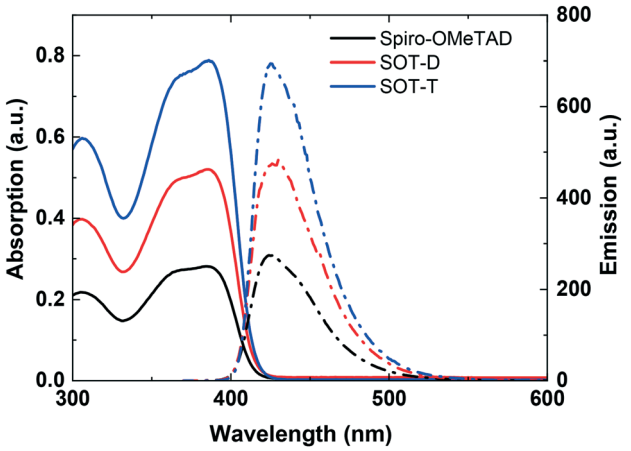

Fig. 1 UV-vis absorption (solid lines) and fluorescence (dashed lines) spectra of **Spiro-OMeTAD**, **SOT-D** and **SOT-T** (CH_2Cl_2, 1.0 × 10^{-5} M). Excitation at λ = 386 nm for fluorescence spectra.

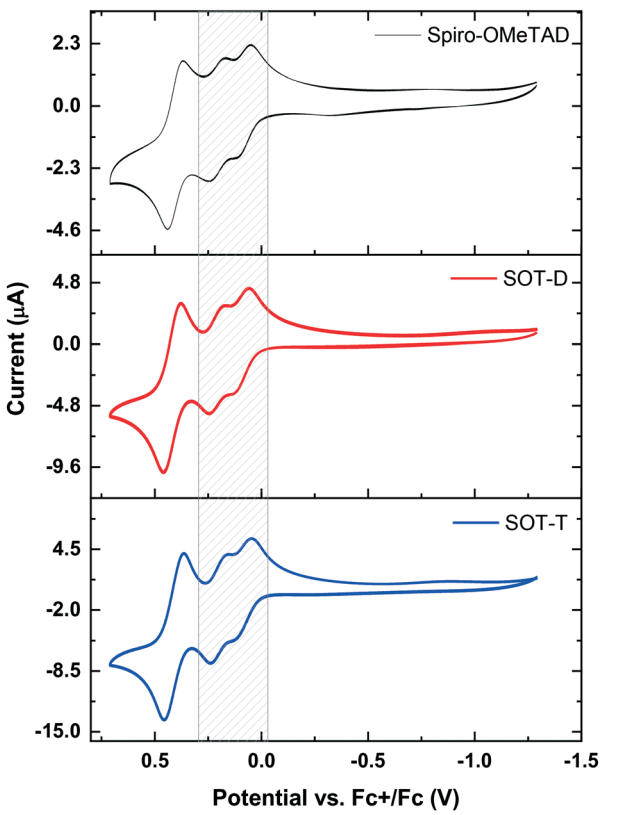

Fig. 2 CVs of **Spiro-OMeTAD**, **SOT-D** and **SOT-T** (CH_2Cl_2, 5 × 10^{-4} M). Conditions: Pt disc working electrode, Pt wire counter electrode, Ag wire pseudo-reference electrode, 0.1 M $TBAPF_6$ electrolyte. Fc^+/Fc was used as external reference.

reversible oxidation event corresponds to a two-electron oxidation from the di-cation to form the fully quinoidal tetra-cation.[33] SWV (Fig. S1, ESI†) allows more accurate determination of the oxidation peaks and ionisation potentials (IP), which for the three compounds are −4.9 eV, which is in good agreement with reported data for **Spiro-OMeTAD**.[36] Similar results were observed by computational studies. The structures of **SOT-D** and **SOT-T** were calculated using density functional theory (DFT) calculations, using the B3LYP hybrid functional and the 3-21G basis set. The results were compared to those of **Spiro-OMeTAD**, obtained with the same level of theory. The highest occupied molecular orbital (HOMO) levels of −4.27 eV, −4.29 eV and −4.26 eV for **SOT-D**, **SOT-T** and **Spiro-OMeTAD**, respectively, were obtained. Although the use of more robust basis sets on **Spiro-OMeTAD** has provided more accurate results,[37] these performance-demanding methods could not easily be applied on the structurally more complex **SOT-D** and **SOT-T**. Nonetheless, this DFT study shows how the HOMO levels of the three molecules are very close to each other, highlighting again the electronic similarities of the three systems, thereby auguring well for future device applications of **SOT-D** and **SOT-T**. The HOMO–LUMO maps (Fig. S2, ESI†) give an idea of the spatial distribution of the frontier molecular orbitals of the three molecules. As expected, the symmetry gives rise to nearly degenerate HOMOs (Table S2, ESI†), two for **Spiro-OMeTAD**, four for **SOT-D** and six for **SOT-T**, all separated by less than 10 meV and spatially delocalised over the side arms and the spiro-centres. The same phenomenon applies to the lowest unoccupied molecular orbitals (LUMOs) which are however spatially more localised over the spiro-centres. A summary of electro-optical properties of **SOT-D** and **SOT-T** compared with **Spiro-OMeTAD** is provided in Table S3 (ESI†).

The thermal properties of **SOT-D** and **SOT-T** were studied by thermogravimetric analysis (TGA) and differential scanning calorimetry (DSC), and compared with **Spiro-OMeTAD**. The results (Fig. 3 and 4) indicate that **SOT-D** behaves very similarly to **Spiro-OMeTAD**, with a mass loss <5%, below 400 °C. **SOT-T** is even more robust with <1% mass lost below 400 °C. Above this temperature they all start to decompose.

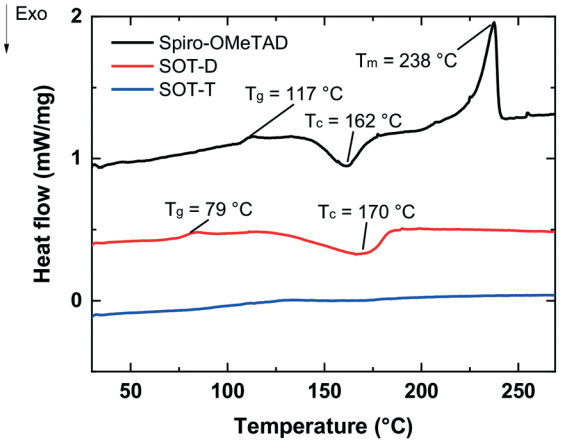

Fig. 4 DSC of **Spiro-OMeTAD**, **SOT-D** and **SOT-T** (first heating wave). Heating rate: 10 °C min^{-1}. Heat flow values were offset for better visualisation.

The DSC analysis of **Spiro-OMeTAD** indicates that it can exist in both amorphous and crystalline forms,[38] as suggested by the presence of a T_g of 117 °C and a crystallisation temperature (T_c) of 162 °C. The melting point (T_m) of the material is identified by the peak at 238 °C. The second heating wave confirmed the presence of the T_g, shifted at 125 °C, while the T_c and T_m were not observed, suggesting that the amorphous phase is more stable than the crystalline (Fig. S3, ESI†). A similar behaviour is shown by **SOT-D**, which exhibits a post crystallisation peak at 170 °C during the first heating cycle, that is not observed during the second heating cycle (Fig. S4, ESI†). A more pronounced T_g is observed at 79 °C, during the first heating wave, and at 121 °C during the second. A different thermal behaviour is shown by **SOT-T** and in particular, the lack of T_c in all cycles suggests that the material is highly amorphous. A T_g at 137 °C is appreciable only during the second heating cycle (Fig. S5, ESI†). This value is higher than that of **Spiro-OMeTAD**, indicating that, in principle, **SOT-T** should have better morphological stability under continuous sunlight exposure.[39]

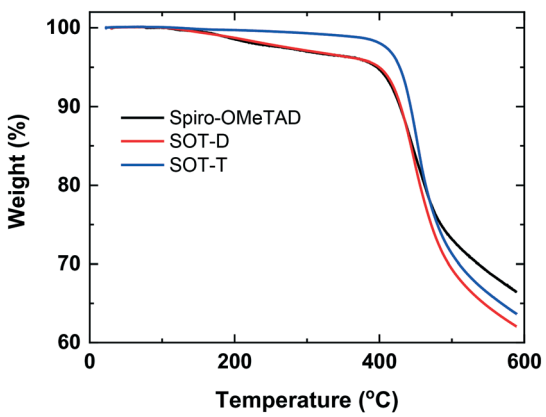

Fig. 3 TGA of **Spiro-OMeTAD**, **SOT-D** and **SOT-T**. Heating rate: 10 °C min^{-1}.

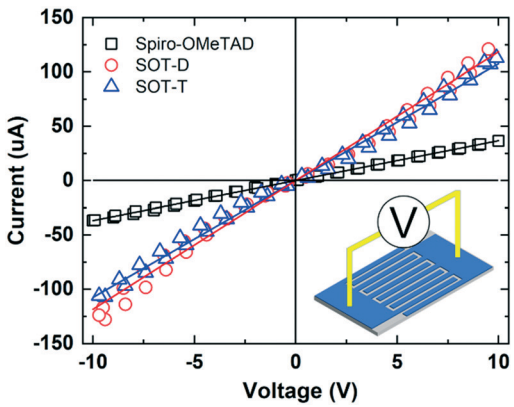

Fig. 5 Current (*I*)–voltage (*V*) characteristics of **Spiro-OMeTAD**, **SOT-D** and **SOT-T**.

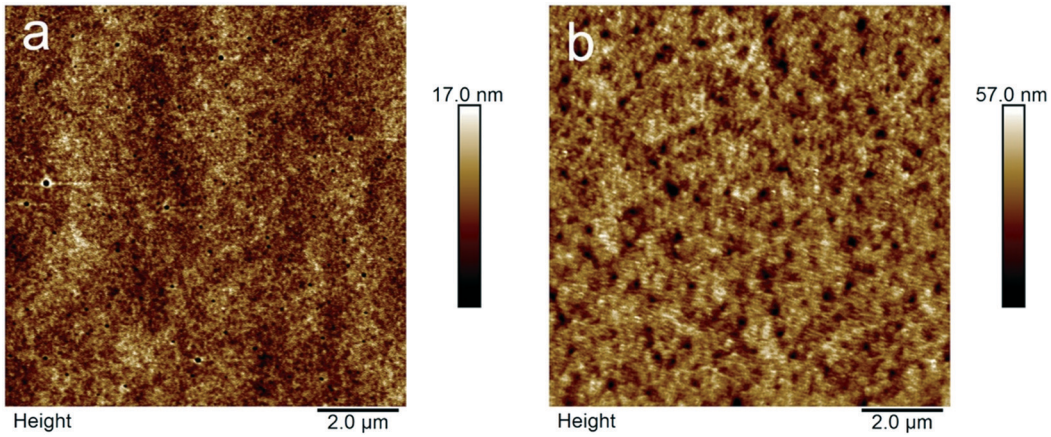

Fig. 6 Tapping mode AFM micrographs of (a) **Spiro-OMeTAD** (Rq = 2.7 nm) and (b) **SOT-D** (Rq = 7.5 nm) films on a glass substrate. Scan area = 10 × 10 μm.

To verify their suitability as hole-transporting materials for solar cells, thin films of these materials were spin coated on patterned ITO substrates including typical additive concentrations and deposited following state-of-the-art perovskite solar cell protocols (detailed device fabrication provided in the ESI†). Their conductivity was extracted from the resistance values of standard current–voltage curves employing an interdigitated electrode pattern, as shown in Fig. 5. To ensure that the resulting HTM films had completed the oxidation process and therefore reach maximum conductivity, the films were left in a desiccator for one week in the dark prior to measuring. The conductivity values obtained for **Spiro-OMeTAD** ($(0.4 \pm 0.1) \times 10^{-4}$ S cm^{-1}) match well with the values reported in the literature.[40,41] Interestingly, **SOT-D** and **SOT-T** demonstrated better conductivity than **Spiro-OMeTAD** throughout. The steeper curves for the **SOT-D** and **SOT-T** clearly demonstrate lower resistance, and conductivity values about 4 times higher ($(1.6 \pm 0.1) \times 10^{-4}$ S cm^{-1}). The higher values could be attributed to higher oxidation rate in these materials as compared to **Spiro-OMeTAD**, as shown by the increase in the oxidised band present at 520 nm in the light absorption spectra (Fig. S6, ESI†).[42,43] We attribute this difference to the more porous nature of our synthesised spiro derivatives, as evidenced in AFM images, (Fig. 6, line plots in fig. S7, ESI†), which increases the available surface area for the oxidation process and thus results in a higher oxidation rate, leading to the observed increase in conductivity. The larger peak-to-trough lateral distances in **SOT-D** films, may be explained by the presence of the spacer groups which may prevent tighter intermolecular packing. Additionally, the increased molecular weight of the dimer, relative to **Spiro-OMeTAD**, can cause reduced solubility, meaning a rougher film is formed due to reduced drying time of solutions undergoing spin-coating.

Further, perovskite solar cells were fabricated to investigate the suitability of these materials as HTMs. Conventional n-i-p device architecture was adopted with FTO/SnO_2 nanoparticles/FAMACs perovskite/HTM/Au stack (experimental details can be found in the ESI†). A mixed cation perovskite with composition $Cs_{0.05}(FA_{0.85}MA_{0.15})_{0.95}PbI_3$ was used as the light absorbing layer. The HTMs were doped with *t*BP and lithium bis(trifluoromethanesulfonyl)imide (LiTFSi) to increase the conductivity and mobility of these materials. The devices were characterised through current–voltage measurements under standard AM1.5 sun illumination. The current density/voltage (*J*/*V*) curves of the best devices are shown in Fig. 7. The devices displayed good performance with 16.47% and 16.01% efficiency for the best **SOT-D** and **Spiro-OMeOTAD** based devices, respectively. The slightly enhanced efficiency value for devices employing **SOT-D** can be attributed to faster oxidation and increased p-doping of the material which can be corroborated with the increased surface area as seen in the AFM images. The data also show slightly enhanced fill factor for the **SOT-D** devices. This suggests that slightly less recombination may occur for **SOT-D** due to its improved conductivity, which is a further benefit of the dimeric HTM. It is often assumed that smoother surfaces are desirable for

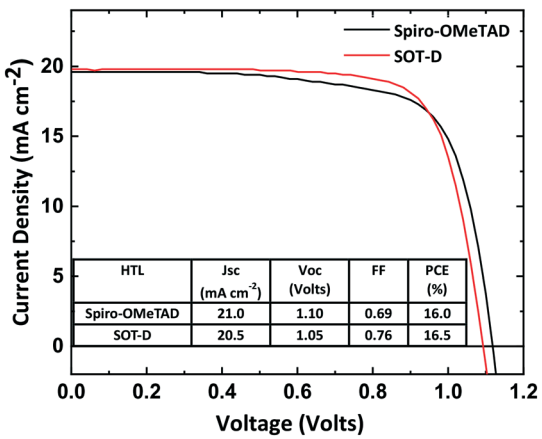

Fig. 7 Current density (*J*)–voltage (*V*) characteristics of devices under one sun illumination (AM 1.5) employing **Spiro-OMeTAD** and **SOT-D** as HTMs.

HTMs, but this study has shown that a more porous film can be used to improve the device performance.

Conclusions

In summary, we report a convenient top-down and a scalable bottom-up procedure for synthesising **SOT-OH**. Furthermore, we report the use of this building block to synthesise **SOT-D** and **SOT-T** by exploiting the reactivity of the hydroxyl group of **SOT-OH**. We have investigated the optical, redox, thermal and optoelectronic properties of **SOT-D** and **SOT-T**, which have shown that these derivatives retain the redox and optical properties of **Spiro-OMeTAD**, whilst in the case of **SOT-T** improved thermal and optoelectronic properties are displayed. We have also shown that **SOT-D** and **SOT-T** have higher conductivity values compared to the parent **Spiro-OMeTAD** which we have attributed to the higher porosity of the dimer and trimer. Likewise, the power conversion efficiencies of perovskite-based devices fabricated using **SOT-D** are higher than those obtained using **Spiro-OMeTAD**, thereby indicating that HTM porosity may also be an important factor affecting device performance. Therefore, this study paves the way for further development of **SOT-OH** for creating a range of new **Spiro-OMeTAD**-based materials for high-performance ss-DSSCs and PSCs, and our progress in this area will be reported in due course.

Author contributions

MC, AHH and FMT synthesised and characterised the compounds and drafted parts of the manuscript and ESI.† PJH and GC devised the synthesis of the materials and contributed to writing the manuscript and ESI.† NP carried out the electronic characterisation of the materials and fabricated the perovskite solar cells, and drafted parts of the manuscript and ESI.† PD oversaw all aspects of the electronic characterisation and device fabrication, interpreted the data and contributed to writing the manuscript and ESI.† JC and PS acquired the AFM images and analysed the resulting data.

Conflicts of interest

There are no conflicts to declare.

Acknowledgements

We thank the EPSRC for funding (GC and AHH EP/P030106/1, PJH EP/P030068/1 and PD EP/T010568/1). We also thank Dr Logan Mackay of the Scottish Instrumentation and Resource Centre for Advanced Mass Spectrometry (University of Edinburgh; Edinburgh, Scotland, UK), for running some of the HRMS. We acknowledge Dr Affar Karimullah for measuring the thickness of the films.

Notes and references

1 U. Bach, D. Lupo, P. Comte, J. E. Moser, F. Weissörtel, J. Salbeck, H. Spreitzer and M. Grätzel, *Nature*, 1998, **395**, 583–585.
2 M. M. Lee, J. Teuscher, T. Miyasaka, T. N. Murakami and H. J. Snaith, *Science*, 2012, **338**, 643–647.
3 H.-S. Kim, C.-R. Lee, J.-H. Im, K.-B. Lee, T. Moehl, A. Marchioro, S.-J. Moon, R. Humphry-Baker, J.-H. Yum, J. E. Moser, M. Grätzel and N.-G. Park, *Sci. Rep.*, 2012, **2**, 591.
4 NREL Best Research Cell Efficiency Chart, **https://www.nrel.gov/pv/cell-efficiency.html**, (accessed March 2022).
5 T. H. Schloemer, J. A. Christians, J. M. Luther and A. Sellinger, *Chem. Sci.*, 2019, **10**, 1904–1935.
6 Z. Hawash, L. K. Ono and Y. Qi, *Adv. Mater. Interfaces*, 2018, **5**, 1700623.
7 C. D. Bailie, E. L. Unger, S. M. Zakeeruddin, M. Grätzel and M. D. McGehee, *Phys. Chem. Chem. Phys.*, 2014, **16**, 4864–4870.
8 G. Divitini, S. Cacovich, F. Matteocci, L. Cinà, A. Di Carlo and C. Ducati, *Nat. Energy*, 2016, **1**, 15012.
9 Y. Kato, L. K. Ono, M. V. Lee, S. Wang, S. R. Raga and Y. Qi, *Adv. Mater. Interfaces*, 2015, **2**, 1500195.
10 N. Rolston, B. L. Watson, C. D. Bailie, M. D. McGehee, J. P. Bastos, R. Gehlhaar, J.-E. Kim, D. Vak, A. T. Mallajosyula, G. Gupta, A. D. Mohite and R. H. Dauskardt, *Extreme Mech. Lett.*, 2016, **9**, 353–358.
11 T. Malinauskas, D. Tomkute-Luksiene, R. Sens, M. Daskeviciene, R. Send, H. Wonneberger, V. Jankauskas, I. Bruder and V. Getautis, *ACS Appl. Mater. Interfaces*, 2015, **7**, 11107–11116.
12 L. K. Ono, S. R. Raga, M. Remeika, A. J. Winchester, A. Gabe and Y. Qi, *J. Mater. Chem. A*, 2015, **3**, 15451–15456.
13 D. Tomkute-Luksiene, M. Daskeviciene, T. Malinauskas, V. Jankauskas, R. Degutyte, R. Send, N. G. Pschirer, H. Wonneberger, I. Bruder and V. Getautis, *RSC Adv.*, 2016, **6**, 60587–60594.
14 M.-D. Zhang, D.-X. Zhao, L. Chen, N. Pan, C.-Y. Huang, H. Cao and M.-D. Chen, *Sol. Energy Mater. Sol. Cells*, 2018, **176**, 318–323.
15 Z. Hu, W. Fu, L. Yan, J. Miao, H. Yu, Y. He, O. Goto, H. Meng, H. Chen and W. Huang, *Chem. Sci.*, 2016, **7**, 5007–5012.
16 M. Saliba, S. Orlandi, T. Matsui, S. Aghazada, M. Cavazzini, J.-P. Correa-Baena, P. Gao, R. Scopelliti, E. Mosconi, K.-H. Dahmen, F. De Angelis, A. Abate, A. Hagfeldt, G. Pozzi, M. Graetzel and M. K. Nazeeruddin, *Nat. Energy*, 2016, **1**, 15017.
17 Y. Shi, Y. Xue, K. Hou, G. Meng, K. Wang, R. Chi, F. Chen, H. Ren, M. Pang and C. Hao, *RSC Adv.*, 2016, **6**, 96990–96996.
18 M.-H. Li, C.-W. Hsu, P.-S. Shen, H.-M. Cheng, Y. Chi, P. Chen and T.-F. Guo, *Chem. Commun.*, 2015, **51**, 15518–15521.
19 Y.-K. Wang, Z.-C. Yuan, G.-Z. Shi, Y.-X. Li, Q. Li, F. Hui, B.-Q. Sun, Z.-Q. Jiang and L.-S. Liao, *Adv. Funct. Mater.*, 2016, **26**, 1375–1381.

20 L. Yang, F. Cai, Y. Yan, J. Li, D. Liu, A. J. Pearson and T. Wang, *Adv. Funct. Mater.*, 2017, **27**, 1702613.
21 A. Magomedov, S. Paek, P. Gratia, E. Kasparavicius, M. Daskeviciene, E. Kamarauskas, A. Gruodis, V. Jankauskas, K. Kantminiene, K. T. Cho, K. Rakstys, T. Malinauskas, V. Getautis and M. K. Nazeeruddin, *Adv. Funct. Mater.*, 2018, **28**, 1704351.
22 X. Jiang, Z. Yu, Y. Zhang, J. Lai, J. Li, G. G. Gurzadyan, X. Yang and L. Sun, *Sci. Rep.*, 2017, **7**, 42564.
23 N. Y. Nia, F. Matteocci, L. Cina and A. Di Carlo, *ChemSusChem*, 2017, **10**, 3854–3860.
24 Z. Zhou, X. Li, M. Cai, F. Xie, Y. Wu, Z. Lan, X. Yang, Y. Qiang, A. Islam and L. Han, *Adv. Energy Mater.*, 2017, **7**, 1700763.
25 M. Li, Z.-K. Wang, T. Kang, Y. Yang, X. Gao, C.-S. Hsu, Y. Li and L.-S. Liao, *Nano Energy*, 2018, **43**, 47–54.
26 J.-M. Wang, Z.-K. Wang, M. Li, K.-H. Hu, Y.-G. Yang, Y. Hu, X.-Y. Gao and L.-S. Liao, *ACS Appl. Mater. Interfaces*, 2017, **9**, 13240–13246.
27 H.-H. Chou, Y.-H. Chiang, M.-H. Li, P.-S. Shen, H.-J. Wei, C.-L. Mai, P. Chen and C.-Y. Yeh, *ACS Energy Lett.*, 2016, **1**, 956–962.
28 M. Freitag, Q. Daniel, M. Pazoki, K. Sveinbjörnsson, J. Zhang, L. Sun, A. Hagfeldt and G. Boschloo, *Energy Environ. Sci.*, 2015, **8**, 2634–2637.
29 S. Pitchaiya, M. Natarajan, A. Santhanam, V. M. Ramakrishnan, V. Asokan, P. Palanichamy, B. Rangasamy, S. Sundaram and D. Velauthapillai, *Mater. Lett.*, 2018, **221**, 283–288.
30 H. Zhang, H. Wang, W. Chen and A. K.-Y. Jen, *Adv. Mater.*, 2017, **29**, 1604984.
31 J. R. Hwu, F. F. Wong, J.-J. Huang and S.-C. Tsay, *J. Org. Chem.*, 1997, **62**, 4097–4104.
32 H. Ashassi-Sorkhabi and P. Salehi-Abar, *RSC Adv.*, 2018, **8**, 18234–18242.
33 W. Zhang, L. Wang, Y. Guo, B. Zhang, V. Leandri, B. Xu, Z. Li, J. M. Gardner, L. Sun and L. Kloo, *Chem. Commun.*, 2020, **56**, 1589–1592.
34 S. Fantacci, F. De Angelis, M. K. Nazeeruddin and M. Grätzel, *J. Phys. Chem. C*, 2011, **115**, 23126–23133.
35 J. García-Cañadas, F. Fabregat-Santiago, H. J. Bolink, E. Palomares, G. Garcia-Belmonte and J. Bisquert, *Synth. Met.*, 2006, **156**, 944–948.
36 W. H. Nguyen, C. D. Bailie, E. L. Unger and M. D. McGehee, *J. Am. Chem. Soc.*, 2014, **136**, 10996–11001.
37 Y. Li, H. Li, C. Zhong, G. Sini and J.-L. Brédas, *npj Flexible Electron.*, 2017, **1**, 2.
38 G. Tumen-Ulzii, C. Qin, T. Matsushima, M. R. Leyden, U. Balijipalli, D. Klotz and C. Adachi, *Sol. RRL*, 2020, **4**, 2000305.
39 L. Calió, S. Kazim, M. Grätzel and S. Ahmad, *Angew. Chem., Int. Ed.*, 2016, **55**, 14522–14545.
40 L. Caliò, M. Salado, S. Kazim and S. Ahmad, *Joule*, 2018, **2**, 1800–1815.
41 S. Kim, S. Bae, S.-W. Lee, K. Cho, K. D. Lee, H. Kim, S. Park, G. Kwon, S.-W. Ahn, H.-M. Lee, Y. Kang, H.-S. Lee and D. Kim, *Sci. Rep.*, 2017, **7**, 1200.
42 J. H. Noh, N. J. Jeon, Y. C. Choi, M. K. Nazeeruddin, M. Grätzel and S. I. Seok, *J. Mater. Chem. A*, 2013, **1**, 11842–11847.
43 U. Bach, Y. Tachibana, J.-E. Moser, S. A. Haque, J. R. Durrant, M. Grätzel and D. R. Klug, *J. Am. Chem. Soc.*, 1999, **121**, 7445–7446.